Anatomy and Flow in Normal and Ischemic Microvasculature Based on a Novel Temporal Fractal Dimension Analysis Algorithm Using Contrast Enhanced Ultrasound

Dimitrios Charalampidis*, Marco Pascotto, Edmund Kenneth Kerut, and Jonathan R. Lindner

***Abstract*—Strategies for improvement of blood flow by promoting new vessel growth in ischemic tissue are being developed. Recently, contrast-enhanced ultrasound (CEU) imaging has been used to assess tissue perfusion in models of ischemia-related angiogenesis, growth-factor mediated angiogenesis, and tumor angiogenesis. In these studies, microvascular flow is measured in order to assess the total impact of adaptations at different vascular levels. High-resolution methods for imaging larger vessels have been developed in order to derive "angiograms" of arteries, veins, and medium to large microvessels. We describe a novel method of vascular bed (microvessel and arterial) characterization of vessel anatomy and flow simultaneously, using serial measurement of the fractal dimension (FD) of a temporal sequence of CEU images. This method is proposed as an experimental methodology to distinguish ischemic from nonischemic tissue. Moreover, an improved approach for extracting the FD unique to this application is introduced.**

***Index Terms*—Contrast enhanced ultrasound (CEU), fractal dimension (FD), ischemia.**

I. Introduction

ABILITY TO assess morphologic changes that occur during neovascularization is becoming increasingly important. Characterization of proliferation and remodeling of noncapillary microvessels (arterioles, venules), small arteries, and small veins is necessary for understanding pathologic alterations in cancer, adaptive responses to tissue ischemia, or therapeutic effects to pro-angiogenic therapies that are now being tested in the clinical setting. Conventional angiography is poorly suited for assessment of the microcirculation due to its limited ability to image vessels $< 100\ \mu$m. In response, there have been recent advances in high-resolution computed tomography or "micro-CT" allowing a detailed three-dimensional mapping of anatomical changes in small arteries and arterioles in animal models of neovascularization related to ischemic disease and atherosclerosis [1], [2]. These studies have been useful for understanding how the normal ordered network or fractal pattern of vessel distribution is disturbed in these pathologic states. However, temporal assessment of vessel territory flow is not possible with these techniques so that the relation between vessel order and flow is not possible.

Contrast-enhanced ultrasound (CEU) imaging has recently been used to assess tissue perfusion in models of ischemia-related angiogenesis, growth-factor mediated angiogenesis, and tumor angiogenesis [3]–[6]. This technique relies on ultrasound detection of encapsulated microbubble contrast agents as they pass through the microcirculation of a tissue within the acoustic beam. Perfusion imaging is performed by destruction of microbubbles within the ultrasound beam profile using high-power imaging sweeps, and then subsequent measurement of the rate and extent of microbubble replenishment back into the sector [7]. In previous studies examining angiogenesis, flow at the most distal portion of the microcirculation has been measured in order to assess the total impact of adaptations at different vascular levels. Recently, high-resolution methods for anatomic mapping of the noncapillary microcirculation have been developed which preserve temporal flow data. These techniques rely on microbubble destruction and subsequent high-frequency real-time imaging using maximum intensity projection (MIP) in order to derive virtual angiograms of arteries, veins and medium to large microvessels. With MIP, the intensity of any given pixel at any time during image acquisition is displayed as the infinite persistence of the maximal intensity achieved.

In this study, we describe a method for assessment of microvessel and arterial flow characteristics using the fractal dimension (FD). The FD has been used in image processing applications including medical applications [8]–[12], and remote sensing [13]. An ability to quantify roughness makes FD analysis particularly useful in texture related applications [14], [15]. In particular, FD has been used for the analysis of ultrasound imagery including that of breast [21], [22], bones [23], atherosclerotic carotid plaques [24], [25], ovarian tumor [26], liver [27], [28], lungs [29], and the backscattering of

Manuscript received December 7, 2005; revised April 25, 2006. *Asterisk indicates corresponding author.*

*D. Charalampidis is with the Department of Electrical Engineering, College of Engineering, University of New Orleans, New Orleans, LA 70148 USA (e-mail: dcharala@uno.edu).

M. Pascotto is with the Division of Cardiology, University of Virginia, Charlottesville, VA 22908 USA.

E. K. Kerut is with the Departments of Physiology and Pharmacology, Louisiana State University Health Sciences Center, New Orleans, LA 70112 USA.

J. R. Lindner is with the Division of Cardiovascular Medicine, Oregon Health and Sciences University, Portland, OR 97201 USA.

Digital Object Identifier 10.1109/TMI.2006.877442

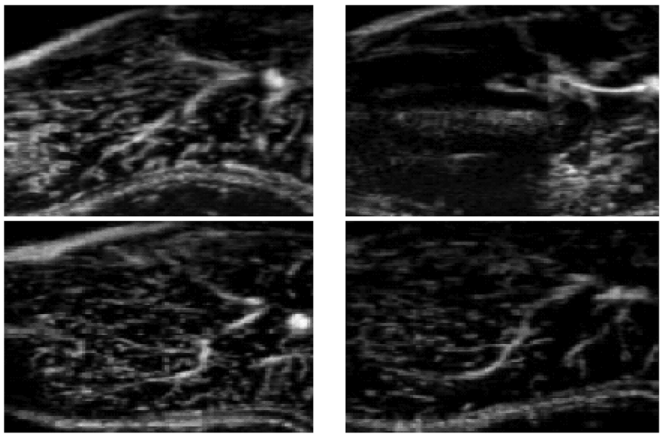

(a) (b)

Fig. 1. Two CEU image examples. Each row shows an example from the same animal for (a) normal and (b) ischemic proximal hindlimbs.

blood cells [30]. Fractal analysis was used in this work because FD has been shown to be successful in describing branching structures [32], [33]. The angiograms of arteries, veins, and microvessels possess textural, and more specifically, branching structure characteristics. Therefore, measurement of the FD appears to be an appropriate measure for quantifying proximal hindlimb ischemia in the laboratory animal. On the other hand, most previous work on texture analysis has shown that other textural descriptors, such as Gabor filter banks and wavelets, seem to be more appropriate for images highly uniform in the textural sense.

A FD-based technique is proposed to study the development characteristics from a sequence of CEU proximal hindlimb images of rats administered microbubble agents, in order to distinguish ischemic from non-ischemic limbs. The novelty of the proposed technique is that, in contrast to static-image FD-based analysis techniques, sequences of images are analyzed by extracting the FD from each image in the sequence and by examining temporal FD development. Moreover, a modification of the *variation* approach [16], [20] for determining the FD in images is introduced suited to the particular application.

This paper is organized as follows. Section II introduces the proposed FD approach and its usefulness to the particular application. Section III presents the animal preparation, the imaging methodology, and the image analysis technique. Section IV presents experimental results evaluating the performance of the proposed fractal measures and comparing them with other measures. Finally, Section V provides a discussion and conclusion.

II. Fractal Dimension Technique

In this section, the FD approach is introduced. Fig. 1 presents examples of CEU hindlimb images obtained from two animals. For each animal, there is one normal [Fig. 1(a)] and one ischemic proximal hindlimb [Fig. 1(b)]. It is noted that normal limbs appear to have a more "organized" and structured vascular anatomy in comparison to ischemic limbs. Therefore, a structure or roughness-based feature is appropriate for the application at hand. In addition, the patterns appear to have a branching structure. Thus, FD is suitable as a method of analysis, as opposed to other textural descriptors.

Section II-A describes the original variation method. Section II-B introduces the modified FD technique, particularly suited for the application of distinguishing between normal and ischemic cases.

A. Variation Method

The variation method is adopted in this paper to compute the FD, since it has been shown to provide more accurate FD estimates for surfaces with a known FD, compared to other commonly used techniques [16], [20]. An $M \times N$ size grayscale image with pixel intensity $Z(x, y)$ at location (x, y) can be considered as a surface of size $M \times N$, with a height of $Z(x, y)$ at (x, y). Let us consider two points $\mathbf{P}_1$ and $\mathbf{P}_2$ on the surface Z. According to the variation method, if a surface Z is a fractal, then the slope of the line passing through points $\mathbf{P}_1$ and $\mathbf{P}_2$ goes to infinity as $\mathbf{P}_1$ approaches $\mathbf{P}_2$. The FD is defined as the rate with which this slope goes to infinity. The variation function is defined as

$$V_\varepsilon(x,y) = \max_{(x',y')\in B_\varepsilon} Z(x',y') - \min_{(x',y')\in B_\varepsilon} Z(x',y') \quad (1)$$

where $(x', y') \in B_\varepsilon$ indicates that the maximum and minimum in (1) are calculated considering pixels located at (x', y') inside a square "box" B_ε of size $(2\varepsilon+1)\times(2\varepsilon+1)$ centered at (x, y). Moreover, $\varepsilon > 0$ is the scale parameter. The rate at which the total variation in Z converges to zero as ε converges to zero is directly related to the FD of Z. The FD of a discrete surface Z is then defined as [20]

$$\mathrm{FD}_\varepsilon = \lim_{\varepsilon\to 0} \frac{\log \sum_{(x,y)\in Z} \frac{V_\varepsilon(x,y)}{\varepsilon^3}}{\log \frac{1}{\varepsilon}}. \quad (2)$$

Practically, the algorithm for calculating the FD of an image is as follows. The variation $V_\varepsilon(x, y)$ is calculated as the difference between the maximum and the minimum grayscale values in a small window of size $(2\varepsilon+1)\times(2\varepsilon+1)$. This window is centered at the image pixel with coordinates (x, y). This computation is repeated for all image pixels (x, y) for different values of ε. If we define E_ε as the sum of the variation $V_\varepsilon(x, y)$ over the whole image, the FD is calculated as the slope of the line that best fits the points $(\log(1/\varepsilon), \log\{(1/\varepsilon)^3 E_\varepsilon\})$ where $\varepsilon = 1, 2, 3, \ldots, \varepsilon_{\max}$. The line that best fits these points can be found using linear regression.

B. Modified Variation Method

It is vital to calculate the FD in a manner that is meaningful for the particular application. The particular hindlimb artery characteristics may bias the FD calculations if the average variation E_ε is used. As mentioned before, the branching structures depicted in the CEU proximal hindlimb images of rats are nonuniform in the textural sense. Let us consider an example of a normal case for which 30% of the microvasculature exhibits slow blood flow and nonsignificant branching, which are characteristics of

an ischemic case. This may be due to the arterial structure of the particular animal. The average variation E_ε will be significantly affected by the ischemic-like 30% of the microvasculature. However, if the median is used, the ischemic-like part of the image will be correctly ignored since the majority of the variations are obtained from the normal areas. Thus, it is imperative to identify a fractal behavior insensitive to the specifics of the hindlimb. This can be achieved if the median variation $MD_\varepsilon = \text{median}(V_\varepsilon(x,y))$ is used instead of the average. The FD of the surface Z will then be defined as

$$\text{FD}_\varepsilon = \lim_{\varepsilon \to 0} \frac{\log \frac{MD_\varepsilon}{\varepsilon^3}}{\log \frac{1}{\varepsilon}}. \tag{3}$$

Nevertheless, utilizing the MD_ε allows the image background to bias the FD calculations. For instance, considering that there exists an approximately constant background, variations $V_\varepsilon(x,y)$ at the background locations for all scales ε will be almost equal to zero. A zero valued background will shift MD_ε to smaller values. In order to avoid the aforementioned problem, the "active" area in the images is defined as the set of pixels in a neighborhood $\aleph$ around nonbackground pixels. In contrast to the original FD where E_ε is calculated over the whole image, MD_ε is calculated only using the pixels in $\aleph$. The nonbackground pixels are determined from the final image in the sequence. The first step in determining the neighborhood $\aleph$ is to use an intensity threshold for removing background noise by setting all background pixels equal to zero. Then, a $L \times L$ size moving average window $W(x,y)$ is employed. The filtered image $Z_f(x,y)$ is equal to $Z(x,y) * W(x,y)$ where $*$ denotes the two-dimensional (2-D) convolution operator. Any nonzero pixel in $Z_f(x,y)$ is considered to be part of $\aleph$. MD_ε is then calculated as the median of all variations calculated in $\aleph$. Similar to the original variation method, the FD is calculated as the slope of the line that best fits the points $(\log(1/\varepsilon), \log\{(1/\varepsilon)^3 MD_\varepsilon\})$ where $\varepsilon = 1, 2, 3, \ldots, \varepsilon_{\max}$.

III. Methodology

A. Animal Preparation

The study protocol was approved by the Animal Research Committee at the University of Virginia. Proximal hindlimb ischemia was produced in 17 Sprague–Dawley rats. Rats were anesthetized with intraperitoneal injection of ketamine hydrochloride (10 mg $\cdot$ kg^{-1}), xylazine (8 mg $\cdot$ kg^{-1}) and atropine (0.02 mg $\cdot$ kg^{-1}). Using an aseptic technique, the left common iliac artery and small proximal branches were ligated. Animals were imaged at days 0, 4, 7, 14, and 28 after surgery. For imaging studies, animals were anesthetized in a similar fashion as above and a jugular vein was cannulated for microbubble administration.

B. Contrast Ultrasound Imaging

Contrast-enhanced ultrasound imaging of the proximal hindlimb was performed in the parasagital plane in the longitudinal orientation of the femoral artery. Phase-inversion harmonic imaging (Aplio, Toshiba Corporation) was performed with a linear array transducer at a receiver frequency of 5.5 MHz and a frame rate of 15 Hz. The dynamic range was set at 40 dB, the acoustic focus was placed at the mid-portion of the hindlimb, and 2-D gains were optimized and kept constant. Contrast enhancement was produced by intravenous injections of approximately 1×10^7 lipid-shelled, decafluorobutane microbubbles (MP1950, University of Virginia). After appearance of contrast in the hindlimb, microbubbles were destroyed by a brief high-power (mechanical index 1.4) pulse sequence. Image sets were then acquired using nondestructive low-power (mechanical index 0.2) imaging using MIP. Data were recorded on magnetic-optical disk, and transferred to a computer for offline analysis.

C. Image Analysis and Temporal Development of Fractal Dimension

Fractal dimension has been extensively used in image analysis and time-series analysis including seismic signals [17], electroencephalograms and electrocardiograms [18], and rain-rate modeling [19]. However, the authors are not aware of studies evaluating the temporal properties and development of branching systems by calculating the FD on still images, which are however part of an image sequence. The only work following a concept similar to our approach is presented in [31] where populations of oligodendrocytes or type 2 astrocytes derived from neonatal rat optic nerves were allowed to differentiate in vitro. The FD of differentiating glial cells was calculated over time. Nevertheless, in addition to the concept of studying the FD development over time being used in a completely different context, the FD in [31] is not directly calculated from the image texture. It is rather estimated from the cellular profiles in order to quantify the complexity of the cellular contours. On the other hand, in our work we use the FD to quantify the branching development of arteries over time. It should also be emphasized at this point, that the proposed FD technique is different than the ones used in time-series analysis. In the case of time-series, the FD is calculated with respect to the time-domain. In our case, the FD is calculated with respect to the spatial-domain. Then, the temporal development of the spatial-domain FD is studied.

Calculating the FD with respect to the time-domain, as in time-series, would not be appropriate for our application. For instance, consider the discrete signal $s(x,y,t)$ constructed from the image sequence using all corresponding pixels located at (x,y). Then, $s(x,y,t)$ is a time domain signal, where x and y are constant while t varies. The FD of $s(x,y,t)$ could be calculated with respect to time t, and the FD average for all pixels (x,y) could be obtained. However, this approach would have the following problems. First, only a single FD measure would be obtained for the whole sequence. Second, there would be a significant problem with alignment of images since the rats are not completely motionless during image capturing. Finally, and perhaps most importantly it can be shown that the signals $s(x,y,t)$ do not exhibit fractal behavior. For instance, if pixel location (x,y) corresponds to an artery, $s(x,y,t)$ would simply be a step function, since it would transition at some point in time from a *no-echo-present* state to an *echo-present* state.

The FD extracted from a sequence of image frames considering examples of both normal and ischemic limbs is depicted in

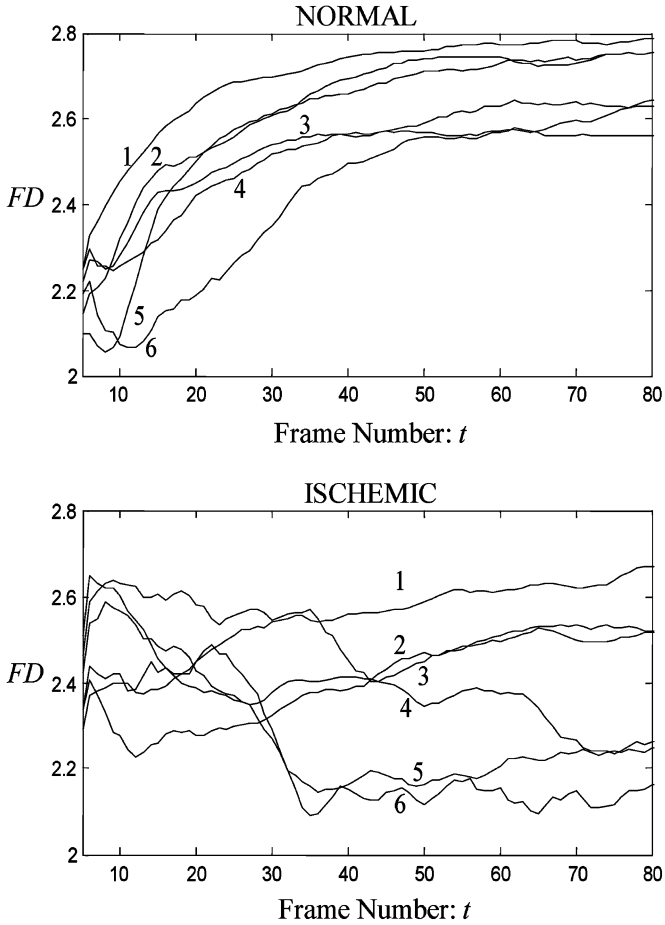

Fig. 2. Development of FD with respect to the frame number for normal and ischemic cases.

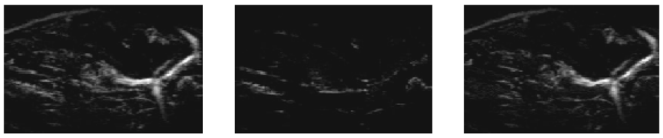

Fig. 3. Example of background subtraction. (a) Image frame. (b) Background frame. (c) Result after subtraction.

Fig. 2. It can be easily concluded that the FD for normal cases exhibits higher increase rate in the beginning of the development compared to the ischemic cases. The results shown in these graphs can be explained since the microvascular flow for the ischemic proximal hindlimbs is expected to indicate a less structured vessel anatomy compared to the normal ones. Therefore, the $\mathrm{FD}(t)$ is an appropriate measure for quantifying ischemia, where t specifies the image frame. On the other hand, a static FD measure will not suffice.

In order to avoid background interference, the first image frame after applying the microbubble destruction by a brief high-power pulse sequence is considered to be the background. The background is subtracted from all consecutive frames in order to obtain images depicting only the microvascular flow. An example of background subtraction is presented in Fig. 3.

After the $\mathrm{FD}(t)$ sequence is obtained, FD features that are capable of differentiating normal from ischemic cases are extracted. These features are selected in order to characterize the flow development as well as the vascular anatomy. More specifically, the following features are used:

$$F_{\mathrm{FD}}^{(i)} = \frac{1}{T} \sum_{t=t_i-T+1}^{t_i} \mathrm{FD}(t). \tag{5}$$

Essentially, $F_{\mathrm{FD}}^{(i)}$ is the average of $\mathrm{FD}(t)$ in the time interval $[t_i - T + 1, t_i]$, where T is the length of the interval and t_i specifies the last point in the interval. The superscript (i) in the feature definition of (5) denotes the ith feature. The $\mathrm{FD}(t)$ curves exhibit a fluctuating behavior, thus the average in (5) is used to increase feature robustness by smoothing the $\mathrm{FD}(t)$ sequence. The T value was empirically chosen to be approximately equal to the period of oscillations. For example, Fig. 2 shows that there is about one oscillation period between frames 50–70 for ischemic curve 6, and between frames 40–60 for ischemic curve 5. This is about 20 frames, corresponding to $T = 1.3$ s for a frame rate of 15 Hz. Considering an $\mathrm{FD}(t)$ sequence of length L_{FD}, a total of I frame numbers t_i may be chosen as shown next

$$t_i = p_i L_{\mathrm{FD}}, \qquad i = 1, \ldots, I \tag{6}$$

Parameters $\{p_i : 0 \leq p_i \leq 1\}$ specify the relative locations, at which features are extracted, with respect to the total length L_{FD} of the $\mathrm{FD}(t)$ sequence. The significance of these features is that they quantify roughness or structure of the CEU images as they develop through time.

IV. Experimental Results

In this section, experimental results are presented to illustrate the importance of the proposed features in the identification of normal and ischemic cases. In this work, four $F_{\mathrm{FD}}^{(i)}$ features are used $(i = 1, \ldots, 4)$, for $p_i = 0.4$, 0.5, 0.6, and 0.8. As a reminder, $t_i = p_i L_{\mathrm{FD}}$. Ideally, time points in the very beginning of the development should show greater differences between the normal and ischemic cases. However, in the early stages of the development, the number of pixels corresponding to visible arteries is small. Thus, the textural image characteristics have not started to form yet, resulting in noisy textural measures.

Fig. 2 shows only 12 out of the 34 curves used in the experiments to illustrate what is intuitively expected: Textural "roughness" increases as branching develops. Since branching of arteries develops faster for normal cases, the $\mathrm{FD}(t)$ should increase faster. Fig. 2 may lead to the conclusion that the slope at early time points could be a better measure than (5). Nevertheless, it was also confirmed in the experiments that this is not generally true for the remaining curves used, and not entirely true even for the curves depicted in Fig. 2. This was expected, since the slope would be especially useful for early time points, however features extracted from those points are noisy in the sense described above. For instance, normal curves 3–6 decrease for the first few frames. Moreover, the $\mathrm{FD}(t)$ may be relatively flat

TABLE I
FOUR PROPOSED FD FEATURES FOR ISCHEMIC AND NORMAL CASES, AND THE FD DIFFERENCES BETWEEN THE FOUR NORMAL AND ISCHEMIC FEATURES

	Ischemic				Normal				Normal – Ischemic			
Rat	$F^{(1)}_{FD}$	$F^{(2)}_{FD}$	$F^{(3)}_{FD}$	$F^{(4)}_{FD}$	$F^{(1)}_{FD}$	$F^{(2)}_{FD}$	$F^{(3)}_{FD}$	$F^{(4)}_{FD}$	$F^{(1)}_{FD}$	$F^{(2)}_{FD}$	$F^{(3)}_{FD}$	$F^{(4)}_{FD}$
1	2.44	2.47	2.46	2.48	2.53	2.57	2.60	2.60	0.08	0.11	0.14	0.12
2	2.47	2.50	2.52	2.53	2.52	2.55	2.57	2.61	0.05	0.05	0.05	0.08
3	2.55	2.55	2.56	2.57	2.58	2.61	2.64	2.69	0.04	0.06	0.08	0.12
4	2.35	2.37	2.38	2.37	2.47	2.52	2.55	2.55	0.12	0.15	0.17	0.19
5	2.27	2.35	2.42	2.53	2.59	2.64	2.67	2.72	0.32	0.29	0.25	0.19
6	2.19	2.24	2.33	2.37	2.35	2.38	2.42	2.55	0.16	0.14	0.09	0.18
7	2.51	2.54	2.57	2.63	2.49	2.55	2.60	2.66	**-0.02**	0.01	0.03	0.03
8	2.41	2.45	2.48	2.54	2.60	2.65	2.67	2.71	0.19	0.19	0.19	0.18
9	2.41	2.42	2.43	2.44	2.54	2.57	2.59	2.65	0.14	0.15	0.15	0.21
10	2.22	2.41	2.56	2.69	2.19	2.27	2.39	2.60	**-0.03**	**-0.14**	**-0.17**	**-0.09**
11	2.46	2.55	2.60	2.67	2.50	2.59	2.63	2.66	0.04	0.03	0.02	0.00
12	2.25	2.33	2.40	2.48	2.43	2.49	2.57	2.63	0.17	0.16	0.17	0.15
13	2.34	2.43	2.49	2.60	2.46	2.56	2.61	2.65	0.13	0.13	0.12	0.05
14	2.36	2.45	2.52	2.63	2.63	2.66	2.68	2.70	0.27	0.21	0.16	0.08
15	2.38	2.46	2.50	2.57	2.63	2.69	2.72	2.74	0.24	0.23	0.22	0.17
16	2.36	2.48	2.57	2.63	2.46	2.54	2.59	2.66	0.09	0.06	0.02	0.03
17	2.37	2.47	2.53	2.61	2.53	2.62	2.66	2.70	0.16	0.15	0.12	0.09
Average	2.37	2.44	2.49	2.55	2.50	2.56	2.60	2.65	0.13	0.12	0.11	0.10
Std. Dev.	0.10	0.08	0.08	0.10	0.11	0.10	0.09	0.06				

for late time points even for normal cases, because the most significant development takes place relatively early. This results in small slopes, although the FD values used to estimate the slopes may be large.

A. Usefulness of the FD Features in Distinguishing Normal From Ischemic Vascularity

In this section, we present results that indicate the ability of the proposed features to distinguish nonischemic from ischemic vascularity from the two proximal hindlimbs of the same rats. Such a comparison partially ignores the effect of the animals' particular vessel anatomy on the feature extraction process. Table I compares the $F^{(i)}_{\mathrm{FD}}$ features extracted from the two different proximal hindlimbs of the same animal. More specifically, the $F^{(i)}_{\mathrm{FD}}$ values for ischemic and normal hindlimbs, and the $F^{(i)}_{\mathrm{FD}}$ feature differences between normal and ischemic hindlimbs for corresponding i values are presented for each animal. As expected, the ischemic cases exhibit lower $F^{(i)}_{\mathrm{FD}}$ values compared to the normal ones with a few exceptions shown in boldface. In most cases, the difference is higher for smaller i values. Small i values are chosen to correspond to the middle stages in the image development where the FD for normal cases has already reached high values while the FD for ischemic cases is still increasing. This conclusion is in agreement to Fig. 2 which illustrates that normal cases reveal faster flow characteristics in the very beginning of the image development compared to the ischemic ones.

Fig. 4(a) presents a plot of feature $F^{(2)}_{\mathrm{FD}}$ versus feature $F^{(1)}_{\mathrm{FD}}$, and Fig. 4(b) presents a plot of feature $F^{(4)}_{\mathrm{FD}}$ versus feature $F^{(3)}_{\mathrm{FD}}$. Fig. 4 shows that the ischemic and normal classes are not completely separable in the feature space. However, there is a good indication that a classifier that uses the $F^{(i)}_{\mathrm{FD}}$ features would be able to reduce classification errors. This is confirmed in the experimental results next.

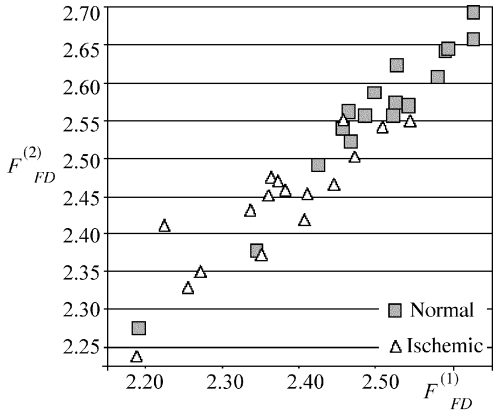

(a)

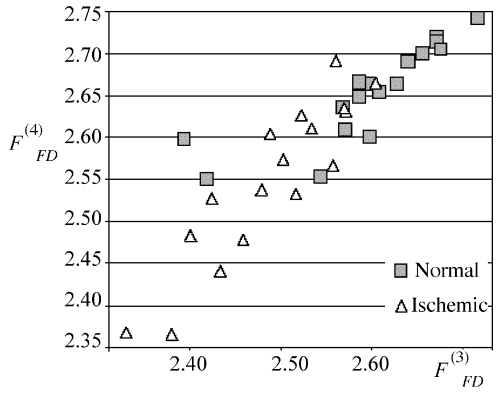

(b)

Fig. 4. Feature plots (a) feature $F^{(2)}_{\mathrm{FD}}$ versus feature $F^{(1)}_{\mathrm{FD}}$, and (b) feature $F^{(4)}_{\mathrm{FD}}$ versus feature $F^{(3)}_{\mathrm{FD}}$.

B. Comparison Between FD and Other Features

In this section, the proposed features are compared with two different feature sets. The first feature set is extracted from the

volume $V(t)$ as it develops through time. The volume is defined as the average pixel intensity in the image, and it is directly related to the arterial flow. There is an indication that the flow for normal cases is faster compared to the ischemic ones, thus $V(t)$ is expected to increase faster and reach a higher value for normal cases. The volume features $F_V^{(i)}$ used for comparison with the FD features are defined as follows:

$$F_V^{(i)} = V(t_i) \tag{7}$$

where t_i is defined as in (6). Four volume features are used for $p_i = 0.2$, 0.4, 0.6, and 0.8 in order to examine the volume development through time, including at early time points. In contrast to texture, the volume increases in a smooth manner starting from the early stages of the development.

The second feature set is calculated from the volume-slope $VS(t)$ which is defined as the slope of $V(t)$ at particular time points. The volume-slope features used for the comparisons are defined as follows:

$$F_{VS}^{(i)} = [V(t_i + T_{VS}) - V(t_i)]/T_{VS}. \tag{8}$$

The $V(t)$ curves are smooth, thus it was found that regression was not needed for the slope calculations. Four volume-slope features are used for $p_i = 0.2$, 0.4, 0.6, 0.8.

In order to assess the performance of the features used, a classification technique, namely the nearest means classifier (NMC), has been employed. More specifically, given a set of data vectors $\hat{x}_{k,l}$ for which the associated classes are known, the mean vector $\hat{m}_k$ and covariance matrix C_k for each class can be calculated as follows:

$$\hat{m}_k = \sum_{i=1}^{N} \hat{x}_{k,l} \tag{9}$$

$$C_k = \sum_{i=1}^{N} (\hat{x}_{k,l} - \hat{m}_k)^T (\hat{x}_{k,l} - \hat{m}_k) \tag{10}$$

where subscript $l = 1, \ldots, N$ denotes the lth feature vector, and subscript $k = 1, \ldots, K$ denotes the kth class. For instance in the FD case, if all four proposed features are used, the data vectors are defined as

$$\hat{x}_{k,l} = \left[F_{\mathrm{FD}}^{(1)} \quad F_{\mathrm{FD}}^{(2)} \quad F_{\mathrm{FD}}^{(3)} \quad F_{\mathrm{FD}}^{(4)} \right]_{k,l}^{T} \tag{11}$$

where subscript l corresponds to the lth animal. Moreover, since there are only two classes, namely ischemic and normal, $K = 2$.

In order to test the feature performance using the NMC, the following procedure is used.

Step 1) All data vectors but one, say $\hat{x}_{k,l_o}$, are used to compute the mean vector and covariance matrix for the two classes, based on (9), and (10).

TABLE II
CLASSIFICATION RESULTS USING THE NEAREST MEANS CLASSIFIER FOR (A) FRACTAL FEATURES AND FEATURE COMBINATIONS, (B) VOLUME FEATURES AND FEATURE COMBINATIONS, AND (C) VOLUME-SLOPE FEATURES AND FEATURE COMBINATIONS

Classification Error (%)					
$F_{FD}^{(1)}$	$F_{FD}^{(2)}$	$F_{FD}^{(3)}$	$F_{FD}^{(4)}$	$F_{FD}^{(1\text{-}3)}$	$All{:}F_{FD}^{(1\text{-}4)}$
23.53	20.59	23.53	32.35	20.59	**14.71**

(a)

Classification Error (%)					
$F_{V}^{(1)}$	$F_{V}^{(2)}$	$F_{V}^{(3)}$	$F_{V}^{(4)}$	$F_{V}^{(1\text{-}3)}$	$All{:}\ F_{V}^{(1\text{-}4)}$
23.53	35.29	26.47	39.29	26.47	**29.41**

(b)

Classification Error (%)					
$F_{VS}^{(1)}$	$F_{VS}^{(2)}$	$F_{VS}^{(3)}$	$F_{VS}^{(4)}$	$F_{VS}^{(1\text{-}3)}$	$All{:}F_{VS}^{(1\text{-}4)}$
41.18	32.35	23.53	47.06	41.18	**32.35**

(c)

Step 2) The data vector $\hat{x}_{k,l_o}$ which was not used in the above calculations is tested. More specifically, the Mahalanobis distance of $\hat{x}_{k,l_o}$ from the two class means ($k = 1, 2$) is calculated

$$d_k = (\hat{x}_{k,l_o} - \hat{m}_k)^T C_k^{-1} (\hat{x}_{k,l_o} - \hat{m}_k). \tag{12}$$

Step 3) Then, vector $\hat{x}_{k,l_o}$ is labeled "class 2" if $d_1 > d_2$, or "class 1" if $d_1 < d_2$. Since the class to which $\hat{x}_{k,l_o}$ actually belongs is known, the correctness of the classification result for $\hat{x}_{k,l_o}$ is also known.

Step 4) Steps 1–3 are repeated for all data vectors $\hat{x}_{k,l}$ and the classification error is recorded.

The classification results are shown in Table II for different features and feature combinations. It is shown that the combination of all four FD features provides smaller classification error compared to any single FD feature, or to the combination of the three features, $F_{\mathrm{FD}}^{(1)}$, $F_{\mathrm{FD}}^{(2)}$, and $F_{\mathrm{FD}}^{(3)}$, or to any non-FD single feature/feature combination.

In order to confirm the superiority of the proposed features, a second comparison approach was followed. More specifically, the features were compared with respect to the separability ratio (SR). The SR is defined as the ratio of the absolute difference between the means of two classes divided by the average standard deviation of the two classes

$$\mathrm{SR} = \frac{|m_1 - m_2|}{(\mathrm{std}_1 + \mathrm{std}_2)/2} \tag{13}$$

where m_1, m_2 and std_1, std_2 are, respectively, the means and standard deviations of the two classes. The numerator of (13) is a measure of the distance between the two classes, and the denominator is a measure of the spread of the two classes. A large SR indicates that the two classes can be better distinguished. Table III shows that all FD features have a higher SR than any other volume or volume-slope feature.

TABLE III
FEATURE COMPARISONS WITH RESPECT TO SR

SR values for features i:	1	2	3	4
$F^{(i)}_{FD}$	1.27	1.43	1.56	1.50
$F^{(i)}_{V}$	0.91	1.03	1.18	1.23
$F^{(i)}_{VS}$	0.89	1.18	0.98	0.88

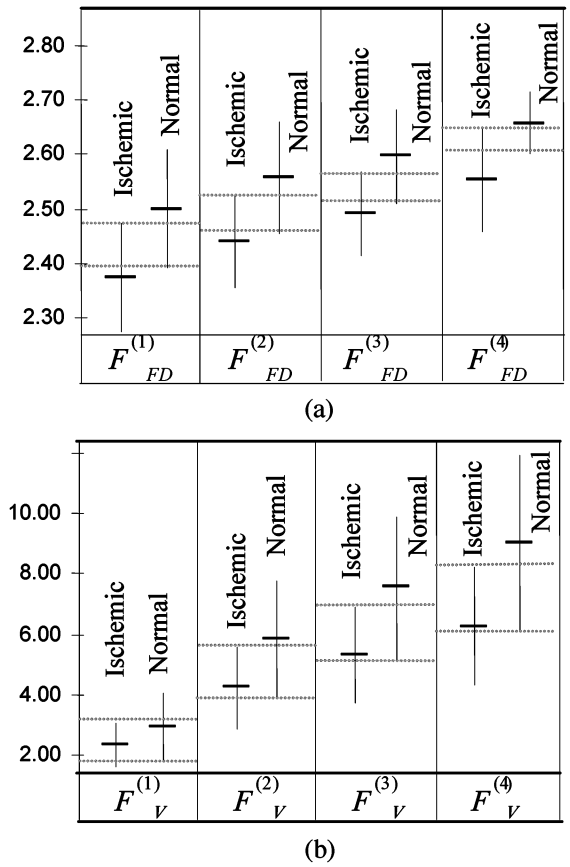

Fig. 5. Averages of the four (a) F_{FD} features, and (b) F_V features, for normal and ischemic proximal hindlimbs. Vertical lines indicate one standard deviation above and below the average. FD ranges from 2 to 3, while the volume ranges from 0 to 100.

Results related to the SR measure are presented in Fig. 5. Fig. 5(a) presents the $F^{(i)}_{\mathrm{FD}}$ feature averages, for the ischemic group and for the normal group. The vertical lines specify one standard deviation above and below the average. Fig. 5(b) presents a similar plot for the $F^{(i)}_{V}$ feature. We notice that in the case of FD, the feature means are at least spaced apart by one standard deviation of either of the two classes. This is not the case for true for $F^{(i)}_{V}$.

V. DISCUSSION AND CONCLUSION

We present a novel algorithm for characterization of vascular anatomy and flow using temporal development of the FD from a sequence of CEU images of the proximal hindlimb in the rat. The novelty of the proposed technique is that the standard Variation technique used for calculating the FD is modified to suit the specific application, and that most importantly this is the first time that the structure of vascular territory is evaluated using such a temporal approach. Although previous works have studied methods for characterizing the anatomical structure, the proposed work provides a study of both anatomy and function. Using this methodology, we have robustly discriminated ischemic from nonischemic limbs. The results presented in Section IV confirm that although FD is appropriate for this application, multiple temporal-based FD features are required in order to achieve fine classification performance. In distinction to this, analysis of temporal average intensity was unable to discriminate these groups.

In conclusion, the temporal FD method proposed in this work appears to be a novel experimental methodology for the analysis and characterization of vascular territories. An interesting direction for future work would be to provide a theoretical relation between the FD measures and the biological vascular models.

REFERENCES

[1] S. H. Wilson, J. Herrmann, L. O. Lerman, D. R. Holmes, Jr., C. Napoli, E. L. Ritman, and A. Lerman, "Simvastatin preserves the structure of coronary adventitial vasa vasorum in experimental hypercholesterolemia independent of lipid lowering," *Circulation*, vol. 105, no. 4, pp. 415–418, Jan. 29, 2002.

[2] X. Y. Zhu, M. Rodriguez-Porcel, M. D. Bentley, A. R. Chade, V. Sica, C. Napoli, N. Caplice, E. L. Ritman, A. Lerman, and L. O. Lerman, "Antioxidant intervention attenuates myocardial neovascularization in hypercholesterolemia," *Circulation*, vol. 109, no. 17, pp. 2109–2115, May 4, 2004.

[3] D. B. Ellegala *et al.*, "Tumor angiogenesis imaging with contrast ultrasound and microbubbles targeted to α_{v}-integrins," *Circulation*, vol. 108, p. 336, 2003.

[4] J. E. Chomas, R. E. Pollard, A. R. Sadlowski, S. M. Griffey, E. R. Wisner, and K. W. Ferrara, "Contrast-enhanced US of microcirculation of superficially implanted tumors in rats," *Radiology*, vol. 229, pp. 439–446, 2003.

[5] H. Leong-Poi *et al.*, "Noninvasive assessment of angiogenesis by ultrasound and microbubbles targeted to α_{v}-integrins," *Circulation*, vol. 107, pp. 455–460, 2003.

[6] H. Leong-Poi, J. Christiansen, P. Heppner, C. Lewis, M. Allieta, A. L. Klibanov, S. Kaul, and J. R. Lindner, "Assessment of endogenous and therapeutic arteriogenesis by contrast ultrasound molecular imaging of integrin expression," *Circulation*, to be published.

[7] K. Wei, A. R. Jayaweera, S. Firozaan, A. Linka, D. M. Skyba, and S. Kaul, "Quantification of myocardial blood flow with ultrasound-induced destruction of microbubbles administered as a constant venous infusion," *Circulation*, vol. 97, pp. 473–483, 1998.

[8] E. R. Edelman *et al.*, "Controlled and modulated release of basic fibroblast growth factor," *Biomaterials*, vol. 12, pp. 619–626, 1991.

[9] C.-C. Chen, J. S. DaPonte, and M. D. Fox, "Fractal feature analysis and classification in medical imaging," *IEEE Trans. Med. Imag.*, vol. 8, no. 2, pp. 133–142, Jun. 1989.

[10] A. I. Penn and M. H. Loew, "Estimating fractal dimension with fractal interpolation function models," *IEEE Trans. Med. Imag.*, vol. 16, no. 6, pp. 930–937, Dec. 1997.

[11] S.-C. Cheng and Y.-M. Huang, "A novel approach to diagnose diabetes based on the fractal characteristics of retinal images," *IEEE Trans. Inf. Technol. Biomed.*, vol. 7, no. 3, pp. 163–170, Sep. 2003.

[12] E. K. Kerut, M. Given, and T. D. Giles, "Review of methods for texture analysis of myocardium from echocardiographic images: A means of tissue characterization," *Echocardiography*, vol. 20, no. 8, pp. 727–736, Nov. 2003.

[13] D. Charalampidis, T. Kasparis, and L. Jones, "Multifractal and intensity measures for the removal of non-precipitation echoes from weather radars," *IEEE Trans. Geosci. Remote Sens.*, vol. 40, no. 5, pp. 1121–1131, May 2002.

[14] T. Kasparis, D. Charalampidis, J. Rolland, and M. Georgiopoulos, "Segmentation of textured images using fractals and image filtering," *Pattern Recognit.*, vol. 34, no. 10, pp. 1963–1973, Oct. 2001.

[15] D. Charalampidis and T. Kasparis, "Wavelet-based rotational invariant segmentation and classification of textural images using directional roughness features," *IEEE Trans. Image Process.*, vol. 11, no. 8, pp. 825–836, Aug. 2002.

[16] B. Dubuc, C. Roques-Carmes, C. Tricot, and S. W. Zucker, "The variation method: A technique to estimate the fractal dimension of surfaces," in *Proc. SPIE, Visual Commun. Image Process. II*, 1987, vol. 845, pp. 241–248.

[17] J. Lingxiu, W. Moon, and W. Kinsner, "Variance fractal dimension analysis of seismic refraction signals," in *IEEE Proc. Commun. Power Comput.*, May 22–23, 1997, pp. 163–167.

[18] J. Olsson and J. Niemczynowicz, "Multifractal analysis of daily spatial rainfall distributions," *J. Hydrol.*, vol. 187, pp. 29–43, 1996.

[19] R. Esteller, G. Vachtsevanos, J. Echauz, and B. Litt, "A comparison of waveform fractal dimension algorithms," *IEEE Trans. Circuits Syst. I, Fundam. Theory Appl.*, vol. 48, no. 2, pp. 177–183, Feb. 2001.

[20] B. Dubuc, J. F. Quiniou, C. Roques-Carmes, C. Tricot, and S. W. Zucker, "Evaluating the fractal dimension of profiles," *Phys. Rev. A*, vol. 39, pp. 1500–1512, 1989.

[21] D. R. Chen, R. F. Chang, C. J. Chen, M. F. Ho, S. J. Kuo, S. J. Hung, and W. K. Moon, "Classification of breast ultrasound images using fractal feature," *Clin. Imag.*, vol. 29, no. 4, pp. 235–245, Jul.–Aug. 2005.

[22] K. G. Kim, S. W. Cho, S. J. Min, J. H. Kim, B. G. Min, and K. T. Bae, "Computerized scheme for assessing ultrasonographic features of breast masses," *Academic Radiol.*, vol. 12, no. 1, pp. 58–66, Jan. 2005.

[23] B. Cortet, N. Boutry, P. Dubois, I. Legroux-Gerot, A. Cotten, and X. Marchandise, "Does quantitative ultrasound of bone reflect more bone mineral density than bone microarchitecture," *Calcified Tissue Int.*, vol. 74, no. 1, pp. 60–67, Jan. 2004.

[24] C. I. Christodoulou, C. S. Pattichis, M. Pantziaris, and A. Nicolaidis, "Texture-based classification of atherosclerotic carotid plaques," *IEEE Trans. Med. Imag.*, vol. 22, no. 7, pp. 902–912, Jul. 2003.

[25] P. Asvestas, S. Golemati, G. K. Matsopoulos, K. S. Nikita, and A. N. Nicolaidis, "Fractal dimension estimation of carotid atherosclerotic plaques from B-mode ultrasound: A pilot study," *Ultrasound Med. Biol.*, vol. 28, no. 9, pp. 1129–1136, Sep. 2002.

[26] A. Kikuchi, S. Kozuma, K. Sakamaki, M. Saito, G. Marumo, T. Yasugi, and Y. Taketani, "Fractal tumor growth of ovarian cancer: Sonographic evaluation," *Gynecologic Oncol.*, vol. 87, no. 3, pp. 295–302, Dec. 2002.

[27] J. Fuite, R. Marsh, and J. Tuszynski, "Fractal pharmacokinetics of the drug mibefradil in the liver," *Phys. Rev. E*, vol. 66, no. 2, Aug. 2002.

[28] M. H. Horng, Y. N. Sun, and X. Z. Lin, "Texture feature coding method for classification of liver sonography," *Computerized Med. Imag. Graphics*, vol. 26, no. 1, pp. 33–42, Jan.–Feb. 2002.

[29] K. N. Prakash, A. G. Ramakrishnan, S. Suresh, and T. W. P. Chow, "Fetal lung maturity analysis using ultrasound image features," *IEEE Trans. Inf. Technol. Biomed.*, vol. 6, no. 1, pp. 38–45, Mar. 2002.

[30] D. Savery and G. Cloutier, "A point process approach to assess the frequency dependence of ultrasound backscattering by aggregating red blood cells," *J. Acoust. Soc. Amer.*, vol. 110, no. 6, pp. 3252–3262, Dec. 2001.

[31] T. G. Smith, Jr., T. N. Behar, G. D. Lange, W. B. Marks, and W. H. Sheriff, Jr., "A fractal analysis of cultured rat optic nerve glial growth and differentiation," *Neuroscience*, vol. 41, pp. 159–166, 1991.

[32] B. R. Masters, "Fractal analysis of the vascular tree in the human retina," *Annu. Rev. Biomed. Eng.*, vol. 6, pp. 427–452, 2004.

[33] J. B. Bassingthwaighte, L. S. Liebovitch, and B. J. West, "Fractal physiology," *Amer. J. Radiol.*, vol. 167, pp. 1185–1187, 1994.